The Effect of Iron Catalyzed Graphitization on the Textural Properties of Carbonized Cellulose: Magnetically Separable Graphitic Carbon Bodies for Catalysis and Remediation.

Jacco Hoekstra,[†] Andrew M. Beale,[‡#$] Fouad Soulimani,[‡] Marjan Versluijs-Helder,[‡] Dirk van de Kleut,[§] Jacobus M. Koelewijn,[†] John W. Geus,[†] Leonardus W. Jenneskens[,†]*

† Organic Chemistry & Catalysis, Debye Institute for Nanomaterials Science, Utrecht University, Universiteitsweg 99, 3584 CG, Utrecht, the Netherlands

‡ Inorganic Chemistry & Catalysis, Debye Institute for Nanomaterials Science, Utrecht University, Universiteitsweg 99, 3584 CG, Utrecht, the Netherlands

UK Catalysis Hub, Research Complex at Harwell, Rutherford Appleton Laboratory, Harwell, Didcot, Oxfordshire, OX11 0FA, UK

$ Department of Chemistry, University College London, 20 Gordon Street, London WC1H 0AJ, UK

§ BASF Nederland B.V. Strijkviertel 67, 3454 PK, De Meern, the Netherlands

* Corresponding author. E-mail: l.w.jenneskens@uu.nl (Leonardus W. Jenneskens), Tel. nr. + 31 30 253 3128

ABSTRACT. Whereas pyrolysis of pristine microcrystalline cellulose spheres yields *nonporous* amorphous carbon bodies, pyrolysis of microcrystalline cellulose spheres loaded with iron salts leads to the formation of magnetically separable *mesoporous* graphitic carbon bodies. The microcrystalline cellulose spheres loaded with either iron(III) nitrate, ammonium iron(III) citrate or iron(III) chloride were pyrolyzed up to 800 °C. Temperature dependent X-ray diffraction analysis shows that the iron salts are transformed into iron oxide nanoparticles; their size and distribution are influenced by the anion of the iron salt. The iron oxide nanoparticles are subsequently carbothermally reduced by the amorphous carbon that is obtained from the pyrolysis of the microcrystalline cellulose. Next, the iron nanoparticles catalyze the conversion of the amorphous carbon to graphitic carbon nanostructures as shown with XRD, electron microscopy and Raman spectroscopy. The extent of graphitization depends on the iron nanoparticle size. Nitrogen physisorption measurements show that this graphitization process introduces mesopores into the carbon bodies. The benefits of the properties of the resulting carbon bodies (ferromagnetic character, graphitic content, mesoporosity) are discussed in connection with applications in liquid-phase catalysis and remediation.

1. Introduction

Activated carbon (AC) finds widespread application as catalyst support [1] and adsorbent for the purification of water and gases [2]. ACs are characterized by a high specific surface area predominantly due to the presence of micropores [3] with an effective diameter of less than 2 nm [4]. They are produced by pyrolysis of natural biomass materials in combination with either physical or chemical activation [5] to introduce porosity. During physical activation the crude material is carbonized followed by activation at elevated temperatures using a mildly oxidizing

2

gas flow (e.g. carbon dioxide, oxygen, steam) [6]. As a consequence, preferential oxidation of some of the charry regions occurs leading to an increase in surface area [3]. In the case of chemical activation the crude material is pre-treated with chemicals, such as phosphoric acid, sulphuric acid or zinc(II) chloride prior to pyrolysis [7] favoring dehydration over depolymerization during the thermal treatment. Consequently, tar formation is restricted. Upon washing the chemicals are removed which results in an AC with high microporosity.

Since ACs are produced from natural materials, their properties (surface chemistry, morphology and, most significantly, porosity) are difficult to control [8]. Notwithstanding these properties are essential for their application as catalyst support [9] or adsorbent [10], in particular for liquid-phase processes in which diffusion and mass transfer coefficients are several orders of magnitude smaller than those in the gas-phase [11].

Transport of reactants and products in catalysis and contaminants in remediation can be further improved by downsizing the AC bodies. The pore lengths will decrease leading to an enhanced transport improving the accessibility of the internal surface area. In addition the pore diameter is important since wider pores enhance the diffusion rate. It is generally agreed that mesopores with a diameter between 2 and 50 nm [4] and macropores with a diameter larger than 50 nm [4] play a crucial role in transport within the AC bodies serving as a passage for either reactants, products or contaminants [12]. Hence, to reduce transport limitations as much as possible the use of small AC bodies with wide pores is preferred.

However, the pressure drop in a fixed-bed reactor in which the AC bodies are generally applied imposes size restrictions (diameter $> 100\ \mu m$) upon these bodies [9]. Although bodies of smaller dimensions down to 3 μm can be used in slurry reactors [13], challenging filtration or ultracentrifugation procedures are required for their isolation. This setback can be alleviated by

3

using magnetic separation [13], i.e. bodies of even smaller dimensions in the nm size range can be employed. In catalysis this will further enhance the contact between the reactants and the catalyst (support) surface [14], while in adsorption the accessible surface area is used much more effectively [15].

Recently we reported the facile preparation of carbon-supported base metal nanoparticles by pyrolysis of microcrystalline cellulose (MCC) spheres homogeneously loaded with the nitrate salts of copper, nickel, cobalt or iron [16]. During pyrolysis under a stagnant inert $N_2(g)$ atmosphere the metal salts are converted to metal oxide nanoparticles. Concomitantly the MCC is converted into an amorphous carbonaceous material. The metal oxide nanoparticles are subsequently carbothermally reduced to metallic nanoparticles. The occurrence of catalytic graphitization by the metal nanoparticles capable of forming metastable metal carbides (nickel, cobalt, iron), was identified as a distinct process that starts at ca. 700 °C [17]. Furthermore, it was found that due to the catalytic graphitization process *mesoporosity* was introduced into the initially *nonporous* amorphous carbon bodies [16]. Catalytic graphitization thus represents an additional activation method besides the generally applied physical and chemical activation approaches for the introduction of porosity into amorphous carbon.

Since iron was found to be the most active graphitization catalyst [17] and also possesses the most attractive properties in view of toxicity, magnetization [18] and cost perspectives, a detailed study on the effect of the iron-catalyzed graphitization on the porosity of the resulting carbon bodies has been performed. By pyrolysis of MCC spheres loaded with various iron salts, the effect of the anion of the ferromagnetic precursor is assessed. The substantial effect the anion has on the iron nanoparticle size and distribution, which dictates the extent of graphitization, was investigated and connected to the introduction of mesoporosity. The presence of the ferromagnetic iron

nanoparticles opens up the perspective of magnetic recovery of the porous graphitic carbon bodies. The benefits of the properties of the prepared carbon bodies (ferromagnetic character, graphitic content, mesoporosity) are demonstrated and the results are discussed in connection with their application in liquid-phase catalysis and remediation.

2. Experimental

2.1. Preparation

2.1.1. Impregnation

Microcrystalline cellulose (MCC) spheres (50 g, Cellets, Syntapharm GmbH, Mülheim an der Ruhr, Germany) of a size range of 100-200 µm were immersed for 24 h in 100 ml 2.0 M aqueous solutions of iron(III) nitrate nonahydrate ($Fe(NO_3)_3 \cdot 9H_2O$), ammonium iron(III) citrate ($C_6H_{11}FeNO_7$, 16.5-18.5 wt.% Fe), or iron(III) chloride hexahydrate ($FeCl_3 \cdot 6H_2O$) under occasional stirring. After filtration over a Büchner funnel with glass filter the samples were dried *in vacuo* at $p = 10^{-2}$ mbar to constant weight.

2.1.2. Pyrolysis

The impregnated spheres (5 g) were pyrolyzed in a stagnant inert N_2(g) atmosphere in a Tube Furnace Reactor (TFR). Prior to pyrolysis the TFR was carefully evacuated and refilled with N_2(g) thrice. Next, the TFR was heated to the desired temperature (500 °C, 600 °C, 700 °C or 800 °C, heating rate 5 °C·min^{-1}, 3 h isothermal). After cooling to room temperature the bodies were exposed to ambient atmosphere.

To demonstrate that scaling-up of the production of the porous ferromagnetic graphitic carbon bodies is viable 100 g of material was prepared in a Fluidized Bed Reactor (FBR, Figure S1, Supplementary Data) in a 1000 ml·min^{-1} flow of N_2(g). Note that FBR's are frequently employed within industry. The reactor was flushed with N_2(g) for 15 min. prior to the pyrolysis process to ensure a pure N_2(g) atmosphere. The FBR was placed in a Sinus Zeist BD 83 furnace. The same pyrolysis procedure was applied as in the TFR using the MCC spheres loaded with ammonium iron(III) citrate.

2.2. Characterization

2.2.1. Thermodynamic Calculations

Thermodynamic equilibria of the hydrogen reduction and the Gibbs free energy of the carbothermal reduction of the relevant iron oxides, taking into account the Boudouard equilibrium ($C + CO_2 \leftrightarrows 2CO$) [19,20], were calculated using a thermo-chemical database (HSC Chemistry 7.1, Outotec Oyj, Finland).

2.2.2. Analyses

Elemental microanalyses were performed by Dornis und Kolbe, Mikroanalytisches Laboratorium, Mülheim an der Ruhr, Germany.

Iron loadings were determined using an IRIS Intrepid II XSP ICP spectrometer. The carbon support was stepwise gasified after which the resulting metal was dissolved in HNO_3 at 80 °C.

Physical adsorption of N_2 at -196 °C using a Micromeritics ASAP 2420 apparatus was used to determine the textural properties of the carbonized materials as a function of temperature. The

specific surface areas and pore size distributions were determined through the Brunauer, Emmet and Teller (BET) [21] and Barret, Joyner and Halenda (BJH) [22] methods, respectively. The presence of micropores was determined from a t-plot analysis [4]. Prior to the measurements the samples were degassed under vacuum for 24 h at 180 °C.

Powder X-ray diffraction (XRD) patterns were obtained with a Bruker-AXS X-ray diffractometer using $CoK\alpha_{12}$ radiation ($\lambda = 0.17902$ nm). For temperature-dependent XRD (TD-XRD) experiments the diffractometer was equipped with an Anton-Paar XRK reaction chamber. To prevent contamination of the reaction chamber by volatile components released from the MCC during pyrolysis, the samples employed in the TD-XRD experiments were dried and preheated at 500 °C for 1 h in the TFR under a stagnant $N_2(g)$ atmosphere (heating rate 5 °C·min^{-1}). During recording of the X-ray diffraction patterns the samples were heated in a He flow (20 l·h^{-1}) to 800 °C with a heating rate of 5 °C·min^{-1} followed by an isothermal treatment at 800 °C for 1 h. The XRD patterns were recorded by continuous scanning from $2\theta = 25\text{-}80°$ for 5 minutes. The temperatures reported are the mid-temperatures of the temperature interval during the measurement. The weight-mean crystallite size (D) was calculated using the Scherrer equation (Eq. 1); $D = 0.94\lambda/(\Delta2\theta\cos\theta)$ in which 0.94 is a constant, λ is the wavelength of the $CoK\alpha_{12}$ radiation, $\Delta2\theta$ is the angular width of the diffraction maximum at half of its maximum intensity (FWHM in radians) and θ is the Bragg angle. The relevant reflections are summarized in Table S1 of the Supplementary Data.

The morphology and local elemental composition of the external surface of the spheres was examined in a Philips XL30 SFEG Scanning Electron Microscope (SEM). The spheres were attached to an aluminum stub by adhesive carbon tape. Secondary electron images provided the morphology of the surface of the spheres. The location of the heavier elements was derived from

Back-Scattered Electron (BSE) images, taken with a solid-state detector. Elemental analysis was executed by recording the spectrum of the emitted X-rays (EDAX software). A FEG Tecnai-20 transmission electron microscope (FEI) equipped with a field-emission gun and a facility for scanning microscopy supplied information about the structure of the thermally treated spheres on a very small scale. The microscope was operated at 200 kV. Samples were prepared by grinding followed by ultrasonic dispersion in ethanol. A drop of the thus prepared dispersion was deposited onto a holey carbon film on top of a copper or nickel grid. A CCD camera at the bottom of the microscope was employed to record lattice images at very high magnification.

Raman spectra were recorded using a $\lambda = 532$ nm diode laser operating at 35 mW and a holoprobe Kaiser Optical spectrometer equipped with a holographic notch filter and CCD camera. Data were collected on an isolated portion of the powdered sample for a period of 30 s over a range of 300–4300 cm^{-1}. The Raman spectra were analyzed using GRAMS/AI software. A multipoint manual baseline subtraction was performed over the entire spectra, and curve fitting was done with the Levenberg-Marquardt algorithm. Peak fitting was performed using mainly Lorentzian functions. Only one band position around 1500 cm^{-1} was best approximated with a Gaussian function. This deconvolution protocol was used before [17] and was a slightly modified literature procedure [23]. To ensure an optimal fit, the spectra were delineated and fitted separately in the first-order (range 800 cm^{-1}-1900 cm^{-1}) and the second-order region (range 2100-3500 cm^{-1}). The first-order region was best fitted with either five or six bands. One band, designated B, represented an artifact of the instrumental setup and was not related to the carbon material (Tables S3-S5, Supplementary Data). The second-order region was best fitted with four bands. When fitting the data, one band in the first-order region (1 cm^{-1}) and one band in the second-order region (2700 cm^{-}

[1]) were constrained to remain within ca. 50 cm^{-1} of their original position. The reduced χ^2 value was used to determine an optimal fit to the data and was below 2% in all cases.

Magnetic hysteresis was recorded at -123 °C using a vibrating sample magnetometer (VSM, Versalab); a range of -15 to 15 kOe was measured. A sample of 4 mg of the material prepared in the FBR was used in this analysis.

The adsorptive properties of the porous ferromagnetic graphitic carbon bodies for the removal of organic contaminants from aqueous solutions were evaluated. Again, the sample prepared in the FBR was used. Figure 1 displays the organic model compound **1** used for these experiments. It is a water-soluble pyrene derivative which was synthesized according to a literature procedure [24]. An excess amount of gaseous trimethylamine was slowly added to a solution of 1-(bromoacetyl)pyrene in dry THF. After 24 h the yellow precipitate was filtered off giving **1** in 72% yield. The adsorption experiment was carried out by adding 5 mg of the adsorbent to 5 ml of a 2 mM aqueous solution of compound **1** in a 1 cm quartz cuvette using a Perkin Elmer Lambda 950 UV/Vis spectrophotometer. The concentration of the supernatant was measured at set time intervals until equilibrium was reached.
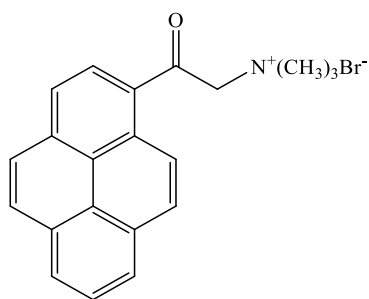

Figure 1. The water-soluble dye 1-trimethyl-(2-oxo-2-pyren-1-yl)-ammonium bromide (**1**) [24].

3. Results and Discussion

3.2. Temperature-dependent XRD

With temperature-dependent XRD (TD-XRD) the reactions occurring during pyrolysis with the loaded MCC spheres were investigated. Note that the samples have been pre-treated under a nitrogen atmosphere at 500 °C for 1 h (see Experimental). Thermal treatment of iron(III) nitrate in air gives Fe_2O_3 [25,26].
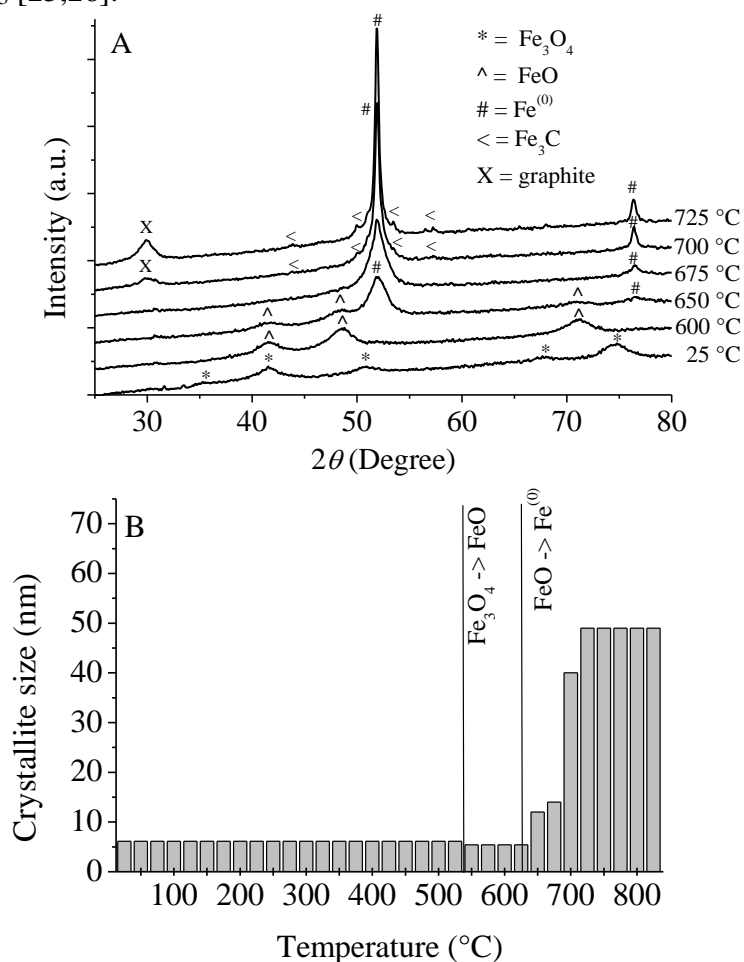

Figure 2. TD-XRD patterns of MCC spheres loaded with iron(III) nitrate after pre-treatment at 500 °C (A) (see also Table S1) and weight-mean crystallite size of the iron-containing particles (B) [16].

In Figure 2A the TD-XRD patterns of the iron(III) nitrate-loaded MCC beads are shown [16]. The 2θ values of the relevant reflections are summarized in Table S1 of the Supplementary Data. Magnetite (Fe_3O_4) nanoparticles were identified with an average crystallite size of ca. 6 nm (Figure 2B), as calculated from the FWHM of the diffraction maxima (Scherrer equation, see Experimental). Raising the temperature induced a stepwise reduction to wüstite ($Fe_{0.96}O$, from now on denoted as FeO) nanoparticles (540-570 °C, weight-mean crystallite size ca. 5 nm). Around 620 °C reduction to metallic iron ($Fe^{(0)}$) starts as indicated by the appearance of *bcc* iron reflections, which has completed at approximately 700 °C. Furthermore, at *ca.* 700 °C low-intensity cementite reflections (Fe_3C) are discernible indicative of carbon uptake by the iron nanoparticles, which become more intense at about 725 °C. Concomitantly, a graphite reflection ($d002$) and an increase in weight-mean iron crystallite size up to *ca.* 50 nm are observed. Note that after these observations the temperature was further raised up till 800 °C in the reaction chamber. However, no additional changes were observed in the XRD spectra, also not after prolonged treatment for 1 h at 800 °C. Therefore it is concluded that the processes observed occur fast, while longer treatment will result in the formation of the same material.

Ammonium iron(III) citrate decomposes at 300 °C in air to hematite (Fe_2O_3) [27], although it has been observed that due to the reducing properties of the thermally decomposing citrate also a large fraction of magnetite (Fe_3O_4) is formed [28]. The thermal pre-treatment in the absence of oxygen is therefore expected to result in magnetite.
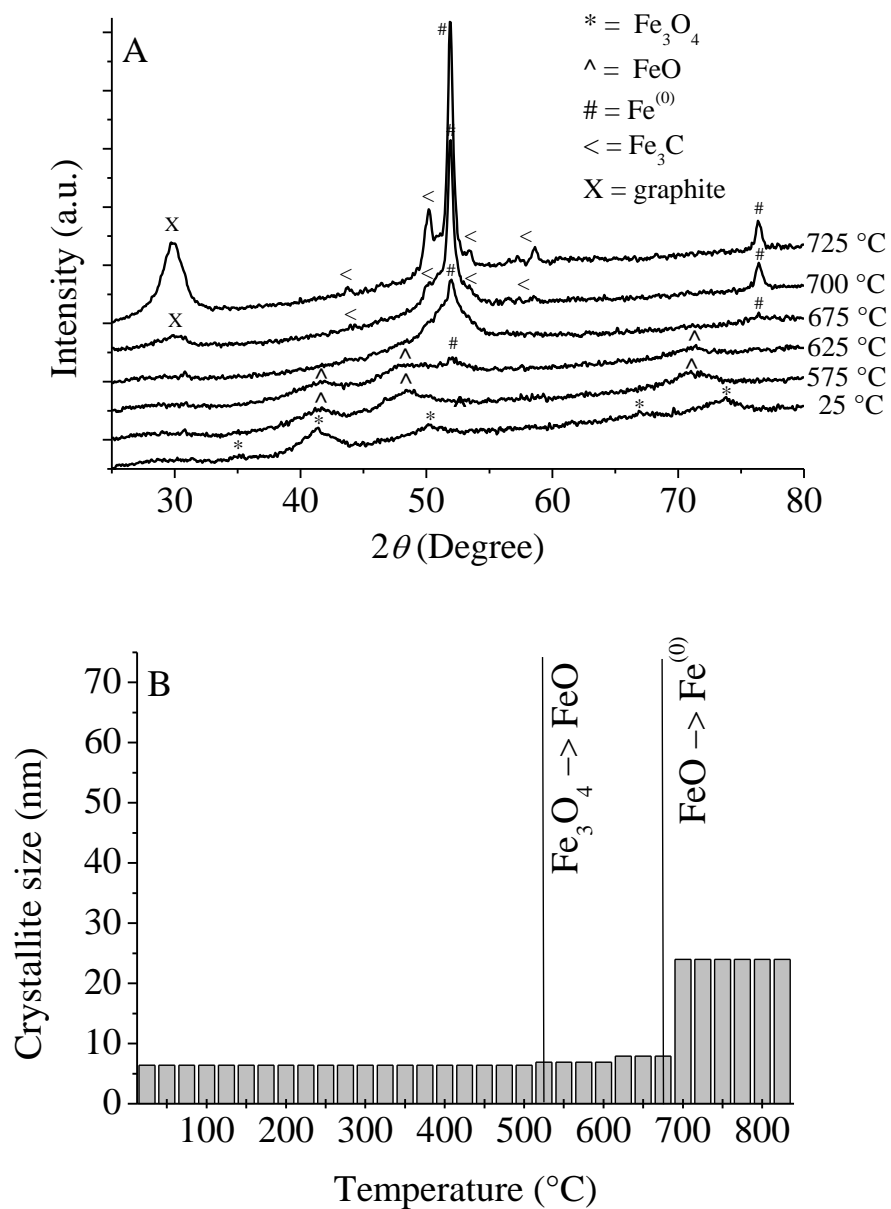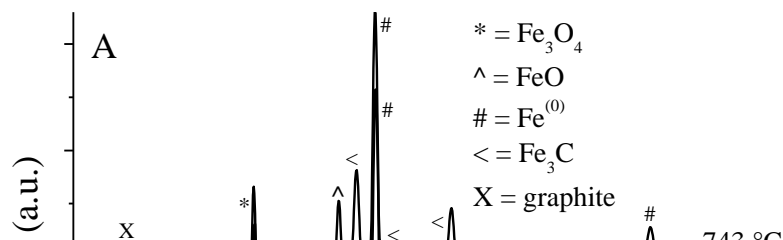
Figure 3. TD-XRD patterns of MCC spheres loaded with ammonium iron(III) citrate after pre-treatment at 500 °C (A) (see also Table S1) and weight-mean crystallite size of the iron-containing particles (B).

Figure 3A represents the XRD patterns measured during the thermal treatment of MCC beads impregnated with ammonium iron(III) citrate. Similar transitions are observed as in the MCC beads loaded with iron(III) nitrate. The pre-treatment at 500 °C leads to magnetite (Fe_3O_4) nanoparticles with a weight-mean crystallite size of *ca*. 6 nm, Figure 3B. Subsequently reduction to wüstite (FeO) at about 525 °C and finally *bcc* iron ($Fe^{(0)}$) occurs at about 625 °C to 675 °C. At *ca.* 700 °C graphite formation is observed which becomes more intense at approximately 725 °C. In addition, also reflections due to cementite (Fe_3C) are discernible at this temperature. After treatment at a temperature above 700 °C the weight-mean crystallite size of the metallic iron particles is *ca*. 24 nm (Figure 3B), which is moderately smaller than in the case of iron(III) nitrate.

Thermal decomposition of iron(III) chloride at 400 °C under ambient conditions leads to Fe_2O_3 at 400 °C [29]. Figure 4A displays the temperature-dependent XRD patterns found upon thermal treatment of MCC beads loaded with iron(III) chloride. To improve interpretability, a scaled version of Figure 4A is shown in Figure 4B.
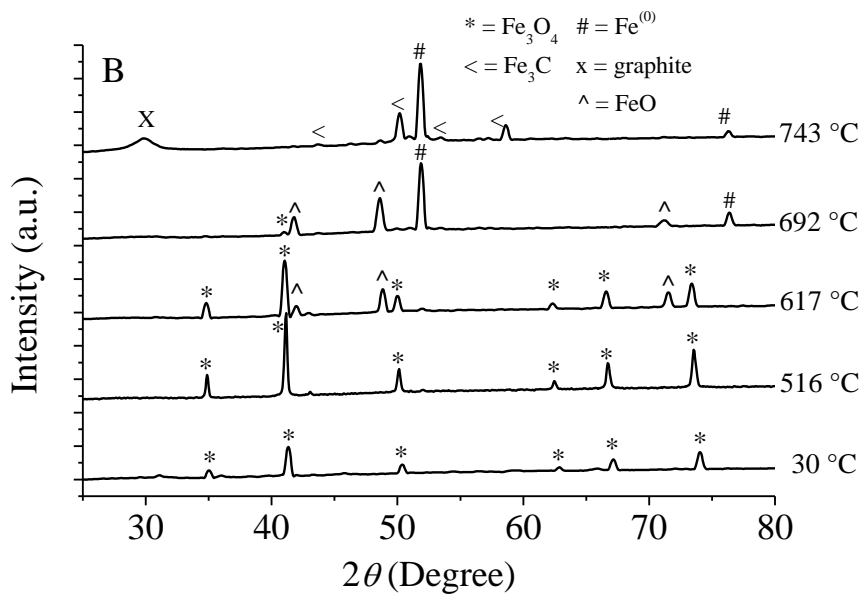

13

Figure 4. TD-XRD patterns of MCC spheres loaded with iron(III) chloride after pre-treatment at 500 °C, original (A) and a scaled version (B) to improve interpretability (see also Table S1).

The XRD pattern recorded at 30 °C shows that after thermal treatment at 500 °C magnetite (Fe_3O_4) is present. The narrow reflections point to the presence of bulk magnetite particles that are much larger than those obtained from the pyrolysis of MCC loaded with either iron(III) nitrate (Figure 2A) or ammonium iron(III) citrate (Figure 3A). Therefore, the weight-mean crystallite size could

14

not be determined. After treatment at 516 °C the reflections due to magnetite increase in intensity. Around 567 °C reduction to wüstite (FeO) starts followed by reduction to *bcc* iron (Fe$^{(0)}$) at about 675 °C, though weak diffraction maxima due to Fe_3O_4 and FeO remain discernable. The co-existence of Fe_3O_4, FeO and Fe$^{(0)}$ is attributed to the larger (bulk) size of the iron containing particles, which delays the reduction. Above 720 °C reduction to metallic iron has completed and the reflections characteristic for graphite and cementite (Fe_3C) become discernable. Note that the intensity of the graphite maximum is considerably lower than that found in the case of ammonium iron(III) citrate and iron(III) nitrate loaded MCC.

3.2. Thermodynamic Considerations

In general, supported iron nanoparticles are prepared by deposition of an iron salt on a hydrophilic support material, such as silica or alumina. Upon calcination iron oxide nanoparticles are formed which are usually stepwise reduced using an external $H_2(g)$ source [30]; the following reduction steps can be observed: $Fe_2O_3 \rightarrow Fe_3O_4 \rightarrow FeO \rightarrow Fe^{(0)}$.

727 °C   227 °C   60 °C   -23 °C

6 —

4 —

2 —

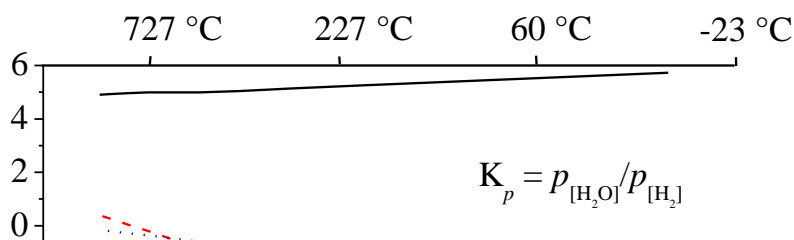$$K_p = P_{[H_2O]}/P_{[H_2]}$$

0 —

15

Figure 5. Thermodynamic equilibria of the reduction of the relevant iron oxides with $H_2(g)$.

However, it is known that the presence of water vapor will strongly affect the rate of reduction and may even prevent the reduction of iron oxides thermodynamically [30-33]. Figure 5 displays the thermodynamic equilibria of the hydrogen reduction of the relevant iron oxides. Since at equilibrium $\Delta G = -RT\ln K_p$, where K_p is the equilibrium constant $K_p = p_{[H2O]}/p_{[H2]}$, the free energy changes for the reduction reactions can be converted into working gas pressure ratios. The equilibria for the equations displayed in Figure 5 were derived from the free enthalpy data in the HSC Chemistry 7.1 database. A more detailed analysis can be found in reference [31]. The data plotted in Figure 5 show that the thermodynamic equilibrium of hematite (Fe_2O_3) and hydrogen shifts, even at high water vapor-to-hydrogen proportions ($K_p = p_{[H2O]}/p_{[H2]}$) to magnetite (Fe_3O_4). Hydrogen reduction to wüstite ($Fe_{0.96}O$, from now on denoted as FeO) and metallic iron requires, however, a much higher temperature, or, at not too elevated temperatures, a low water vapor-to-hydrogen ratio. Due to its hydrophobicity activated carbon (AC) is therefore an attractive support for metallic iron nanoparticles. The water released during reduction will be readily removed from the hydrophobic surface.
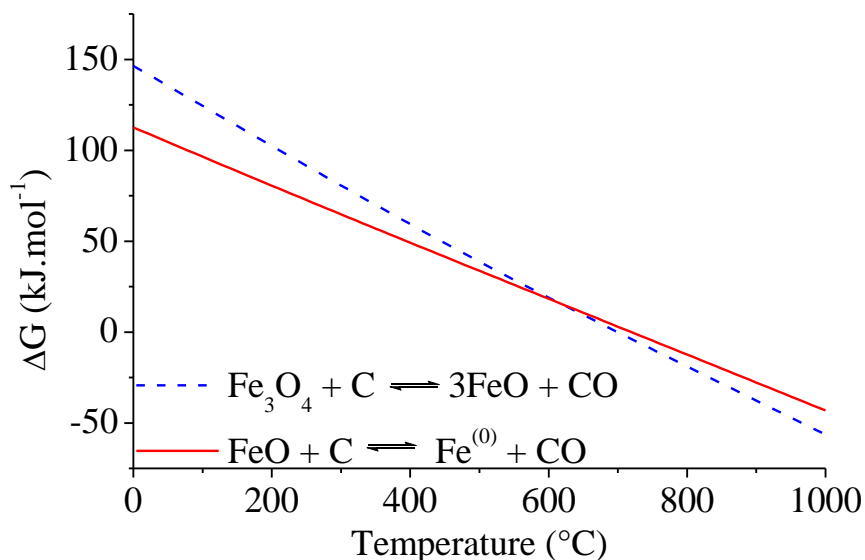
Figure 6. Gibbs free energy of the carbothermal reduction of the relevant iron oxides.

Although hydrogen reduction of the various iron oxides is possible, from a sustainability and safety perspective it is more attractive to make use of a carbothermal reduction process in which the carbon reductant originates from renewable materials such as cellulose. A recent review affirms that this approach has become more popular over the past few years to produce metal functionalized nanostructures [34]. In Figure 6 the Gibbs free energies as a function of temperature of the carbothermal reduction reactions of the relevant iron oxides (*vide infra*) are displayed. These calculations indicate that the stepwise carbothermal reduction of $Fe_3O_4 \rightarrow FeO \rightarrow Fe^{(0)}$ are thermodynamically favorable, respectively, at 700 °C and 720 °C. Whereas thermal treatment of cellulose initially releases water and carbon dioxide, hydrogen, carbon monoxide and char (amorphous carbon) are formed at higher temperatures [35]. Elemental analysis of the carbonaceous products after pyrolysis at such temperatures of pristine MCC has shown that it essentially consists of (amorphous) carbon (Table S2, Supplementary Data) [16,17]. As shown with the temperature dependent XRD results, cellulose is an attractive precursor that provides the carbon support and acts as the carbothermal reducing agent for the preparation of carbon-supported

iron nanoparticles by pyrolysis of iron salt loaded MCC spheres. The calculated temperatures of carbothermal reduction firmly agree with those experimentally observed, which gives credence that the mode of reduction is indeed a carbothermal one.

3.3. Electron Microscopy
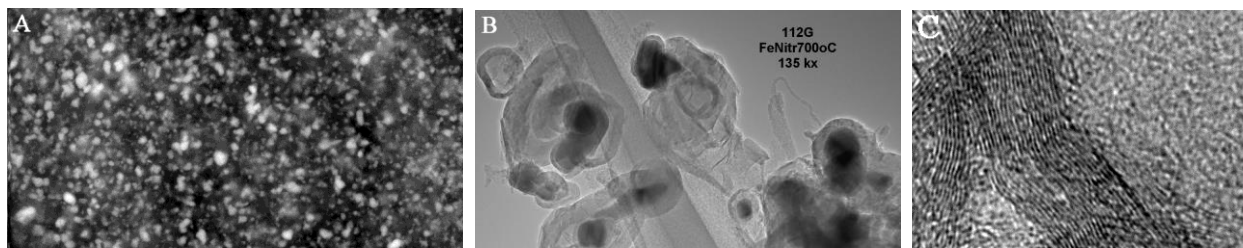
4,5

Figure 7. SEM-BSE (A), TEM (B) and HR-TEM image (C) of MCC spheres loaded with iron(III) nitrate after pyrolysis at 700 °C; SEM-BSE (D), TEM (E) and HR-TEM image (F) of MCC spheres loaded with ammonium iron(III) citrate after pyrolysis at 700 °C; SEM-BSE (G), SEM-BSE (H) and HR-TEM image (I) of MCC spheres loaded with iron(III) chloride after pyrolysis at 500 °C, 800 °C and 800 °C, respectively.

Figure 7 represents electron microscopy images of MCC loaded with iron the respective iron salts after pyrolysis. The SEM-BSE image of Figure 7A shows the external surface of MCC spheres loaded with iron(III) nitrate after pyrolysis at 700 °C. Iron nanoparticles are relatively homogeneously distributed. The recrystallization of the initially amorphous carbon [17] to

graphitic carbon is apparent from the curved graphitic layers as observed with TEM (Figure 7B) and HR-TEM (Figure 7C). The iron nanoparticles appear to be encapsulated by graphitic layers. The iron nanoparticles formed upon carbothermal reduction are able to take up carbon atoms as an interstitial iron carbide as evidenced by the appearance of cementite reflections in XRD. Since graphitic carbon is thermodynamically more stable than iron carbide, graphitic nanostructures are subsequently formed [16,17].

Figure 7D shows a SEM-BSE image of the external surface of a bead loaded with ammonium iron(III) citrate after pyrolysis at 700 °C. Similar to the beads loaded with iron(III) nitrate, iron nanoparticles are homogeneously spread over the surface of the spheres. Again, the amorphous carbon is converted to ribbons of graphitic carbon as observed with TEM (Figure 7E) and HR-TEM (Figure 7F). Furthermore, encapsulation of the iron nanoparticles by multiple graphitic layers also occurs.

Previously we reported on the catalytic graphitization effect of various transition metals [17]. With metals that were carbothermally reduced at relatively lower temperatures (e.g. nickel below 500 °C and cobalt around 570 °C), the formation of a thin graphite-like shell surrounding the reduced nanoparticles was observed. At more elevated temperature, due to the difference in the thermal expansion coefficients of the metallic core compared to its surrounding shell, pressure develops which eventually led to rupture of the graphite-like shell. The metallic core flows out and starts to recrystallize the amorphous carbon to nanostructured graphitic material with a ribbon morphology. With iron the situation appears to be more complex. We attribute this to the higher temperature of carbothermal reduction of around 700 °C at which the mobility of the iron particles is much higher. Encapsulation within graphitic shells and the formation of ribbon-like graphitic

nanostructures appears to occur simultaneously. Figures 7B and 7E also both show empty graphitic shells that appear to be previously occupied by reduced iron cores.

Figure 7G shows a SEM-BSE image of beads loaded with iron(III) chloride and thermally treated at 500 °C; a strongly heterogeneous distribution of magnetite (TD-XRD, Figure 6) species results. The surface of some beads is almost completely covered with large magnetite particles, whereas other beads in Figure 7G exhibit a much lower coverage with fairly large magnetite particles. Thermal treatment at 800 °C leads to large iron particles formed at the external surface of the beads as shown in the SEM-BSE image of Figure 7H. The formation of large iron particles when using MCC beads loaded with iron(III) chloride is ascribed to the volatility and deliquescent character of iron(III) chloride [36]. The iron(III) chloride volatized from the loaded MCC spheres during pyrolysis, which led to Ostwald ripening of the deposited iron species. Since the volatility of the smaller iron chloride(III) particles will be higher than that of the larger particles, this will lead to transport to the larger particles. This is further validated by an independent experiment in which samples of MCC spheres loaded both with either iron(III) nitrate or iron(III) chloride were positioned at opposite sides of the TFR and pyrolyzed simultaneously. Deposits of large iron particles onto the surface of both MCC spheres were found attributed to cross-contamination in which iron species from the MCC loaded with iron(III) chloride volatized and deposited onto the surface of the MCC loaded with iron(III) nitrate [37]. It should be noted that although a relatively intense graphite reflection is observed with the TD-XRD experiments, graphite formation is only locally observed with HR-TEM (Figure 7I). In addition, also amorphous carbon is observed. The degree of graphitization is lower than in the case of MCC spheres loaded with either iron(III) nitrate or ammonium iron(III) citrate (see also section 3.4., Raman spectroscopy).

3.4. Raman Spectroscopy

Raman spectroscopy is highly sensitive to detect short-range disorder in carbonaceous materials and was therefore employed to obtain more detailed information about the catalytic graphitization process observed with XRD and electron microscopy. Pyrolysis of pristine MCC yields amorphous carbon in the temperature range employed [17]. The Raman spectra of carbon materials consist of various bands [23]. Two bands at 1580 cm^{-1} (G-band) and 1350 cm^{-1} (D1-band) dominate the first-order spectrum (range 800-1900 cm^{-1}) [38]. The G-band is indicative for an ideal graphitic lattice vibration of the in-plane bond stretching motion of pairs of sp^2 hybridized carbon atoms [39]. In small sized crystallites the D1-band is present around 1350 cm^{-1}, which reflects disorder in the system. This band is ascribed to either defects or edges in the graphitic lattice, and is characteristic for the in-plane breathing vibrations of sp^2 bonded carbon within structural defects. The edges of graphitic crystallites are represented by a low-intensity band around 1610 cm^{-1} (D2) [40], and usually appears as a shoulder of the G-band. A few low-intensity bands around 1500 cm^{-1} (D3) and 1200 cm^{-1} (D4) complete the first-order Raman spectrum, which point to an amorphous carbon [41,42] and C-C and C=C vibrations [43]. The second-order spectrum (range 2100-3500 cm^{-1}) consists of 4 bands [41]. The overtone of the D1 band (2×D1) around 2700 cm^{-1} is important as it is sensitive to the stacking of graphitic layers [44]. The second-order spectrum is completed with a combination band at 2900 cm^{-1} (G+D1) and overtones at 3100 cm^{-1} (2×D2) and 2400 cm^{-1} (2×D4).
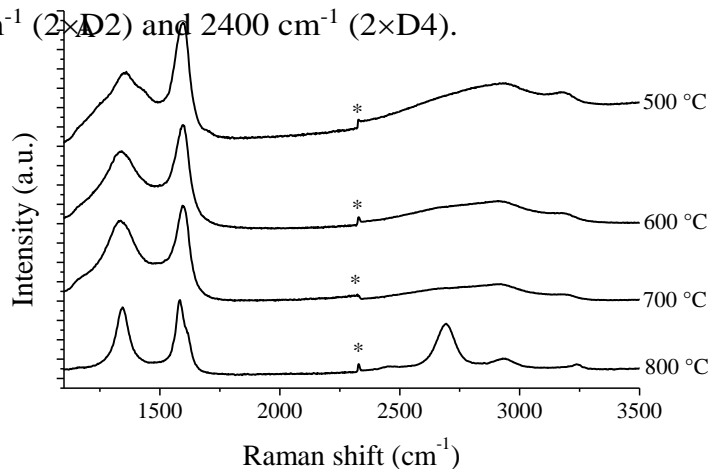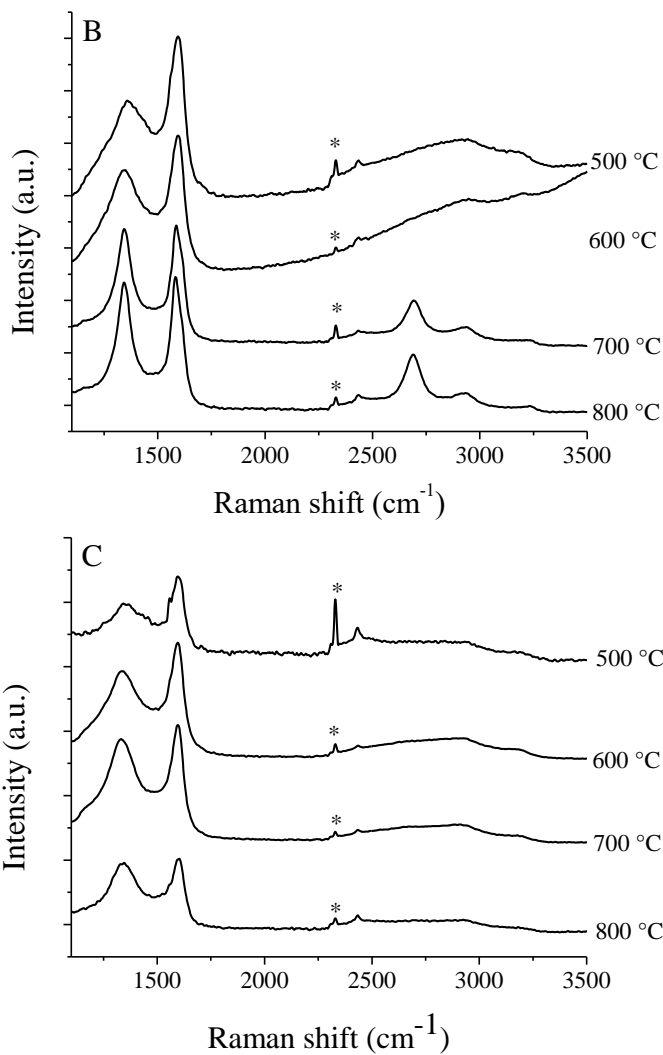
Figure 8. Raman spectra of the carbon bodies obtained after pyrolysis loaded with iron (III) nitrate (A), ammonium iron(III) citrate (B) and iron(III) chloride (C), * = $N_2(g)$.

The Raman spectra of the MCC beads after pyrolysis are shown in Figure 8. The deconvolution results are summarized in Tables S3-S5 of the Supplementary Data. The results of the iron(III) nitrate loaded beads support the outcome of the temperature-dependent XRD and electron microscopy study. Up to a pyrolysis temperature of 700 °C the Raman spectra point to the presence

of a highly disordered amorphous carbon. The G- and D1-bands are broad, while the G-bands are positioned around 1596 cm^{-1} (Table S3), a shift to higher wavenumbers compared to its natural position at 1580 cm^{-1}. This shift is explained by the highly disordered nature of the amorphous carbon phase obtained. The small graphitic domains have a high proportion of edges. Therefore the D2-band becomes dominant [45,46] and subsequently merges with the G-band into a single band with a shift to the position of the D2 band. After pyrolysis at 800 °C, however, marked differences are observed for both the first- and second-order spectra. In the first-order spectrum both the D1- and G-band are much sharper with respect to the Raman spectra obtained at lower temperatures. The position of the G-band is shifted to 1582 cm^{-1} while the D2-band is clearly observed as a shoulder at 1616 cm^{-1}. The most striking change is observed in the 2nd order Raman spectrum. Particularly, the 2×D1 band situated at 2692 cm^{-1} becomes prominent and sharpens (FWHM = 90 cm^{-1}). For highly crystalline graphite a double band would have been expected [44]. The single band feature points to a turbostratic stacking of the graphitic material which means that there is no interlayer interaction between the adjacent graphitic layers. An interlayer spacing larger than 3.42 Å is defined as being turbostratically stacked. In these cases the Raman spectrum resembles that of monolayer graphene [47]. Indeed broadening of the 2×D1 band has been observed earlier for turbostratic graphite, although to a lesser extent (45-60 cm^{-1}) [48] than here observed.

   With ammonium iron(III) citrate similar observations are made as with iron(III) nitrate. The main difference is that the graphitization process is already observed at 700 °C (sharpening of D1- and G-bands, appearance of the D2-band in the first-order spectrum, and appearance of the 2xD1 band at 2700 cm^{-1}, Figure 8B). Graphitization thus occurs at a slightly lower temperature than in the case of iron(III) nitrate, which is tentatively ascribed to a slightly lower reduction temperature

of the iron species due to the reducing effect of the citrate. Furthermore the same behaviour is observed as in the case of iron(III) nitrate.

With iron(III) chloride the Raman spectra merely point to the presence of amorphous carbon at all temperatures investigated. The D1- and G-bands remain broad and an isolated D2 band is not observed (Figure 8C). Sharpening of the bands in the second-order spectra is also not observed indicating that a largely amorphous carbon is obtained. These results support the lower amount of graphitic carbon being formed with iron(III) chloride as detected with XRD and electron microscopy and is attributed to the lower catalytic activity of the larger iron particles formed with iron(III) chloride as precursor (see also sections 3.2. and 3.3.).

3.5. Textural Properties

3.5.1. BET Surface Areas and BJH Pore Size Distributions

In Table 1 the textural properties of the samples obtained after pyrolysis as determined with nitrogen physisorption are summarized. The BET surface areas and BJH pore size distributions of the pristine MCC spheres after pyrolysis could not be determined. Hence, they possess a very low surface area implying that a material without inner porous surface has been formed. Therefore, these MCC spheres represent an ideal model system to assess the influence of catalytic graphitization on the textural properties of the carbon materials obtained after pyrolysis.

**Table 1.** Textural properties of the impregnated and thermally treated beads.

Sample	BET SA[a] $(m^2 \cdot g^{-1})$	V_{micro}[b] $(cm^3 \cdot g^{-1})$	V_{meso}[c] $(cm^3 \cdot g^{-1})$
MCC – 800 °C	n.d.	n.d.	n.d.

Iron(III) nitrate - 500 °C	121	0.03	0.04
Iron(III) nitrate - 600 °C	103	0.03	0.06
Iron(III) nitrate - 700 °C	315	0.09	0.08
Iron(III) nitrate - 800 °C	177	0.01	0.43
Iron(III)-citrate - 500 °C	n.d.	n.d.	n.d.
Iron(III)-citrate - 600 °C	n.d.	n.d.	n.d.
Iron(III)-citrate - 700 °C	219	0.02	0.45
Iron(III)-citrate - 800 °C	204	0.01	0.44
Iron(III)-chloride - 500 °C	n.d.	n.d.	n.d.
Iron(III)-chloride - 600 °C	n.d.	n.d.	n.d.
Iron(III)-chloride - 700 °C	451	0.16	0.01
Iron(III)-chloride - 800 °C	456	0.16	0.01

[a] Surface area according to the BET theory, [b] Micropore volume estimated from a t-plot analysis

[c] Mesopore volume according to the BJH method , n.d. = could not be determined due to low surface area.
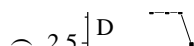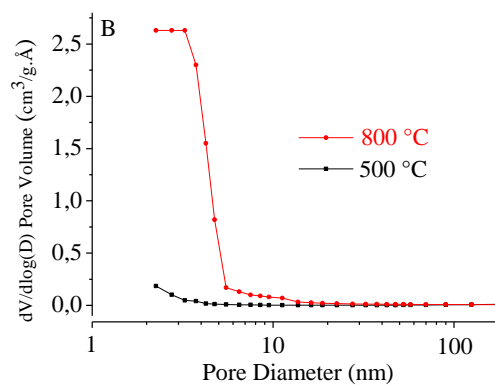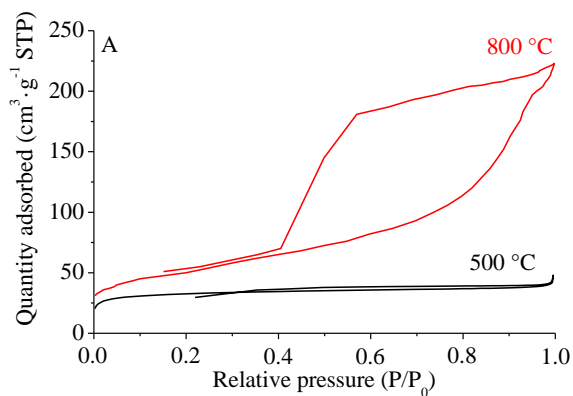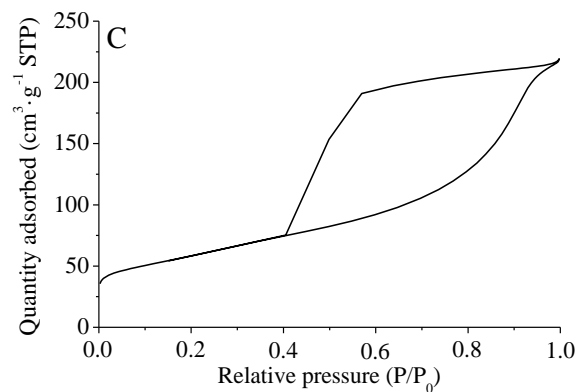
Figure 9. Adsorption-desorption isotherms of MCC beads loaded with iron(III) nitrate after pyrolysis at 500 °C (type I) and 800 °C (type IV) (A) and BJH pore size distributions (B); adsorption-desorption isotherm (type IV) of MCC beads loaded with ammonium iron(III) citrate after pyrolysis at 800 °C (C) and BJH pore size distribution (D); adsorption-desorption isotherm (type I) of MCC beads loaded with iron(III) chloride after pyrolysis at 800 °C (E) and BJH pore size distribution (F).

With iron(III) nitrate loaded beads largely microporous carbons were obtained at the lower pyrolysis temperatures (500-700 °C, Table 1), with increasing surface area with temperature, although some mesopores are also present. The adsorption-desorption isotherm (Figure 9A, 500

°C) exhibits a type I [9] hysteresis curve indicative for a microporous solid. Presumably the release of NO_x during the iron(III) nitrate decomposition is responsible for the partial oxidation of the cellulosic and/or amorphous carbon support upon pyrolysis at 500-700 °C [49], as the pristine spheres are non-porous upon pyrolysis (*vide supra*). Upon reduction to metallic iron and subsequent graphitization of the carbonaceous support material the microporosity collapsed (> 700 °C) in favor of mesopore formation (Table 1). In this process the surface area drops, while the pore volume increases. The adsorption-desorption isotherm (800 °C, Figure 9A) shows a characteristic type IV [9] hysteresis loop due to capillary condensation of nitrogen taking place in mesopores. The BJH pore size distribution (Figure 9B) confirms that mesopores are introduced during the conversion of amorphous carbon to graphitic carbon, while these are virtually absent prior to graphitization. The average pore diameter was found to be 4.2 nm. Note that the BJH method to obtain pore size distributions is only valid for mesopores.

A non-porous carbon is obtained upon pyrolysis of MCC beads loaded with ammonium iron(III) citrate at the temperatures before reduction to metallic iron (500 °C and 600 °C, Table 1). Upon reduction of the iron species and the concomitant appearance of graphite (as shown with TD-XRD, HR-TEM and Raman spectroscopy) a mesoporous carbon material was obtained with a surface area of 219 $m^2 \cdot g^{-1}$ and 204 $m^2 \cdot g^{-1}$ after pyrolysis at 700 °C and 800 °C, respectively (Table 1). In the adsorption-desorption isotherm (800 °C, Figure 9C) again a characteristic type IV [9] hysteresis loop is observed due to capillary condensation of nitrogen taking place in mesopores. Also here mesopores were introduced by the catalytic graphitization process as shown by the BJH pore size distribution of Figure 9D, with a reported average pore diameter of 4.1 nm.

The BET surface area and porosity of the carbonaceous materials obtained from the pyrolysis of MCC beads loaded with iron(III) chloride at 500 °C and 600 °C could not be measured due to their

low surface area. Upon reduction, however (700-800 °C), a high surface area is obtained due to the formation of micropores as summarized in Table 1. The adsorption-desorption isotherm (Figure 9E) exhibits a type I hysteresis indicative for a microporous solid with a relatively small external surface area. The uptake of nitrogen is governed by the accessible micropore volume. This microporosity is introduced via a chemical activation process induced by the iron(III) chloride. ACs are commonly activated by chemical treatment with, for example, zinc(II) chloride, and subsequent pyrolysis. During heat treatment of cellulose-like materials pre-treated with zinc(II) chloride, a Lewis acid, dehydration is favored over depolymerisation yielding a microporous AC [50]. Iron(III) chloride, also being a Lewis acid, has the same function. As a result the yield of the material left upon thermal treatment of MCC impregnated with iron(III) chloride is ca. 30-40 wt.%, which is higher than the yield of beads impregnated with iron(III) nitrate or ammonium iron(III) citrate (18-25 wt.%, Table S6, Supplementary Data, yields and metal loadings of MCC beads after pyrolysis). This results in a lower metal loading for the iron(III) chloride-loaded beads compared with the iron(III) nitrate-loaded beads. The lower loading of the iron(III) citrate-loaded beads stems from the sub-stoichiometric amount of iron present in the ammonium iron(III) citrate (16.5-18.5 wt.%, see Experimental). Note that during isothermal pyrolysis the loss of carbonaceous material from both the pristine as well as the loaded MCC spheres increases with the temperature of pyrolysis [16]. Therefore, an increase of metal content is observed for the loaded MCC with increasing temperature. The lack of graphite formation in the case of iron(III) chloride, and, consequently, the lower mesopore volume (see also the BJH pore size distribution of Figure 9F), is attributed to the heterogeneous distribution and larger size of the resulting iron particles after pyrolysis; the larger particles being less active in the catalytic graphitization process. Mesopore formation is therefore hampered.

3.5.2. Modifying Textural Properties Using Catalytic Graphitization

Porosity in ACs is usually introduced either via chemical or physical activation. Catalytic activation of carbon precursors using either metal salts or organometallic compounds has been attempted [51,52], although the resulting porosity has generally not been associated with the catalytic graphitization process as illustrated in the examples below. In one example an organometallic cobalt precursor was mixed with a phenolic resin. The resin was spun to fibers, which were carbonized at 900 °C under an $N_2(g)$ atmosphere. Loss of mechanical strength of the fibers was attributed to the formation of graphite. Upon subsequent steam activation mesopores were observed, the formation of which was ascribed to accelerated oxidation at the cobalt species [53]. Unfortunately, the authors did not measure the adsorption of N_2 at -196 °C prior to steam activation. The effect of the graphitization process on the porosity was therefore not established. In another example an AC was impregnated with cobalt and pyrolyzed at 900-1000 °C in a H_2-Ar flow. Methane and graphite formation were observed. The formation of mesopores, however, was attributed to excavation of the AC by migrating cobalt particles and not to the generation of graphite [54]. Zhai *et al.* combined chemical activation using zinc(II) chloride with catalytic graphitization by iron and nickel of mesophase pitch [55]. The microporosity collapsed in favor of pores of a larger diameter. The surface area dropped rapidly with an increase in the temperature of thermal treatment (700 - 900 °C) and apparently with the extent of graphitization, although the introduction of mesoporosity was again not ascribed to the formation of graphite. In a recent effort iron catalyzed graphitization of biomass (sawdust) led to mesoporous carbon materials containing graphitic nanostructures [56]. The porosity of the carbonized biomass in the absence of iron catalysts, however, was not reported. In the above examples we believe that the introduction of

mesopores can be attributed to the catalytic graphitization induced by the metal nanoparticles. The elegance of the MCC spheres used in this study is that pyrolysis of the unloaded MCC spheres yields a *nonporous* carbonaceous material. Therefore, the influence of the catalytic graphitization on the mesopore formation was assessed indisputably, in contrast to the studies mentioned above.

When looking at the average pore diameters of the graphitized materials of roughly 4 nm, there seems to be a discrepancy with the iron particle size obtained after pyrolysis (50 and 24 nm for iron(III) nitrate and ammonium iron(III) citrate, respectively, see Figures 2 and 3). Note however, that upon the final reduction step to *bcc* iron ($Fe^{(0)}$) nanoparticles, their size is approximately 6 nm. These are the nanoparticles that are active in the catalytic graphitization process transforming the amorphous carbon to graphitic carbon. While migrating through the amorphous carbon the iron nanoparticles sinter upon contacting other iron nanoparticles yielding larger sized iron nanoparticles. Also sintering via migration of the iron nanoparticles over the smooth graphitic surfaces formed cannot be excluded. The average pore diameter thus nicely agrees with the size of the iron nanoparticles obtained via carbothermal reduction.

3.6. Applications of the Porous Ferromagnetic Graphitic Carbon Bodies.

3.6.1. Scale-up

Several factors are pivotal for the application of the ferromagnetic mesoporous graphitic carbon bodies. First of all the feasibility to scale-up the production of the materials must be investigated, since for the various applications envisioned large volumes of material are required. An

advantageous aspect of our approach is that it is not required to introduce a reducing agent as a gas flow in scale up experiments. Passing a reducing gas flow through a fixed bed (e.g. external $H_2(g)$) generally leads to a reduction front where the reaction almost exclusively proceeds, while the upstream part of the bed is exposed to the reduction product, which is usually water vapor. With cellulose as the carbon precursor for the carbothermal reduction the reducing agent is present throughout the bed and in intimate contact with the iron species; transport is therefore not an issue. Scale-up experiments (100 g) were performed in which the MCC spheres impregnated with ammonium iron(III) citrate were pyrolyzed in a Fluidized Bed Reactor (FBR, Figure S1, Supplementary Data). Note that FBR's are frequently applied in industry. During pyrolysis, a $N_2(g)$ flow was applied (see Experimental). A general risk in the use of FBR's is attrition of the bodies. The carbonized MCC bodies however, remained intact under the flow conditions applied, which indicate that they are fairly strong. Since graphite acts also as a lubricating agent, attrition of the carbon bodies does not proceed significantly [57]. Satisfactorily, the analytical data (XRD, nitrogen physisorption, electron microscopy and Raman spectroscopy) showed no difference between samples prepared in the TFR and the FBR.

3.6.2. Ferromagnetic Character

For application in catalysis and remediation the increased mesoporosity of the carbon bodies is favorable facilitating the transport of reactants, products and/or contaminants in- (and out of) the bodies, which is particularly important in liquid-phase processes with low diffusion and mass transfer coefficients [11]. Utilization of even smaller bodies will be attractive to even further lower

transport limitations towards the surface as well as within the support bodies themselves. This can be achieved making use of their intrinsic ferromagnetic character. Magnetic separation and isolation of very small bodies (10-20 nm) can be performed readily and swiftly [14,58]. Iron is the most practical of the ferromagnetic species due to its high saturation magnetization (222.6 emu·g$^-$^{1}) and Curie temperature (770 °C) [18]. This enables an easy separation of the bodies and ensures that the bodies can be kept magnetically in suspension at elevated temperatures provided that the iron is protected from the environment so that oxidation is prevented. Furthermore, it is beneficial that iron is cheap and non-toxic. Moreover, for reuse it is important that the porous ferromagnetic graphitic carbon bodies have no remanence.
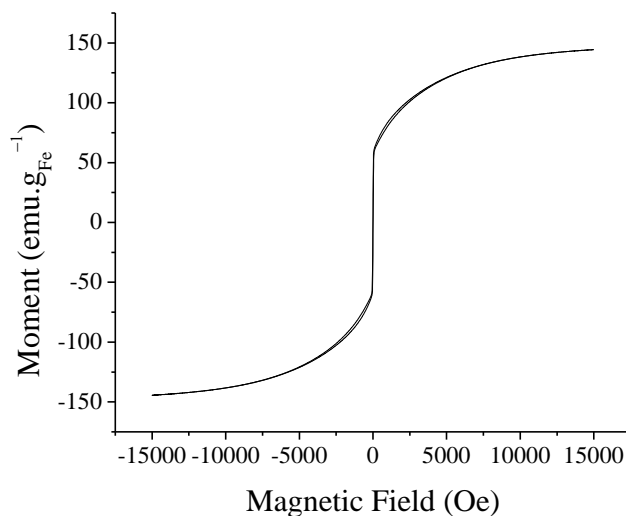

Figure 10. Magnetic hysteresis loop measured at -123 °C of MCC beads loaded with ammonium iron(III) citrate after pyrolysis at T 800 °C (FBR).

Figure 10 shows the magnetic hysteresis loop for the ferromagnetic carbon bodies prepared in the FBR (MCC, ammonium iron(III) citrate, N_2(g), 800 °C) recorded at -123 °C between -15 and 15 kOe. Electron microscopy (Figure 7E) revealed that the iron nanoparticles within the carbon bodies are at least partly encapsulated within a graphitic envelope. Hence, these particles are protected from ambient atmosphere and therefore from oxidation and subsequent loss in magnetic

moment. Also the presence of cementite enhances the stability of the ferromagnetic character [59]. Whereas unsupported zero-valent iron nanoparticles are pyrophoric [60] this is not the case with these carbon-supported iron nanoparticles. The hysteresis loop for the ferromagnetic carbon bodies shows a saturation magnetization of 144 emu.g_{Fe}^{-1}, which is lower than the saturation magnetization of bulk iron. The lower saturation magnetization is attributed to the presence of cementite (Fe_3C, Figure 5), with a saturation magnetization of 140 emu.g_{Fe}^{-1} [61]. The value found is indeed within the range of the saturation magnetizations found for iron carbide nanomaterials [62]. Also surface oxidation of the iron nanoparticles that were not completely encapsulated within a graphitic envelope may partly account for a lower saturation magnetization.

Magnetic hysteresis was insignificant, which implies that the remanence (the magnetization remaining after removal of the external magnetic field) and the coercive force (the magnetic field strength to be applied in the direction against the initial magnetizing field to effect a zero magnetization) [63] were negligible. In connection with their application the low remanence is of importance as magnetic aggregation does not occur in the absence of an (inhomogeneous) magnetic field; clustering of the bodies is therefore prevented. Upon dispersion of the ferromagnetic carbon bodies in solution in water, the bodies can easily be isolated with an externally applied magnetic field. (See movie S1, Supplementary Data). Upon removal of the magnetic field, the bodies are indeed easily redispersed in water, confirming their magnetically soft character.

3.6.3. Catalysts and Magnetically Separable Catalyst Supports

For catalysis the porous ferromagnetic graphitic carbon bodies can be employed in two ways; as catalysts themselves or catalyst supports. The relatively small iron particles present in the carbon

bodies that represent a considerable free surface area allows for application in catalysis. Alternatively, when the ferromagnetic graphitic carbon bodies are merely used as magnetically separable catalyst supports for catalysts other than iron, the iron component has to be excluded from the reaction mixture.

Though catalysts with metallic iron are employed in industrially important processes as the ammonia [64] and Fischer-Tropsch synthesis [65], the fact that the hydrogen reduction of iron oxide asks for either very low water vapor pressures or very high temperatures (Figure 2) resulted in the fact that the ammonia synthesis catalyst developed around 1910 is still almost exclusively employed. This catalyst contains rather large iron particles of about 30 to 50 nm. The ferromagnetic graphitic carbon bodies we obtained in the scale-up experiments contain many very small iron particles (ca. 25 nm) and expose therefore a substantial metallic iron surface per unit weight of catalyst. The relatively low density of the catalyst bodies ensures that settling of the catalyst in liquids does not proceed rapidly, which is advantageous for the use in slurry reactors. The iron nanoparticles present in the graphitic carbon bodies are therefore a promising candidate in the field of catalysis.

The accessibility of the iron nanoparticles for reactants was therefore assessed using a 4M HCl solution. Clearly, some of the iron content has dissolved, as observed by the rapid color change of the HCl solution to yellow, showing the accessibility of part of the iron nanoparticles for reactants (see also reference 16).

The bodies after the 4M HCl treatment, however, remained magnetic, indicating that part of the iron component was protected from the 4M HCl solution attributed to the formation of the graphitic envelopes (Figure 7E). The technology to apply catalytically active precursors to the graphitized carbon has been developed for carbon nanofibers [66]. It is also possible to anchor (non-

covalently) homogeneous catalysts [67] or organocatalysts [68] onto the surface of the beads as shown with cobalt nanoparticles coated with a graphitic coating prepared via spray pyrolysis. Utilization of very small ferromagnetic support bodies can lead to transport within the bulk of the liquid approaching that attainable with homogeneous catalysts. By magnetic means the very small catalyst bodies can still be readily separated from the liquid. Re-dispersion of the catalyst bodies after magnetic separation is also readily achieved (movie S1, Supplementary Data). The bodies developed can thus also be employed as magnetically separable catalyst support. The size of the bodies can be tuned either by ball-milling of the ferromagnetic graphitic carbon bodies or by using MCC spheres of smaller dimensions.

3.6.4. Remediation

The ferromagnetic graphitic carbon bodies developed can also be used as adsorbents in liquid-phase processes. The surface area within the carbon bodies is well accessible due to the presence of mesopores. The adsorptive properties of the bodies were therefore tested in the removal of organic impurities from water. The water-soluble dye containing a pyrene moiety (**1**) was therefore used as a model compound (Figure 1). This dye was designed for the non-covalent functionalization of carbon nanotubes containing graphitic surfaces at their exterior, since pyrene is known to have a high affinity for graphitic surfaces via π-π stacking interactions [68]. We therefore suspected that the developed mesoporous adsorbents containing graphitic carbon were well-suited for the removal of compound **1** from aqueous solution. An adsorption experiment was carried out in a UV/Vis cuvette in which 5 ml of a 2 mM aqueous solution was exposed to 5 mg of the ferromagnetic graphitic adsorbents prepared in the FBR. The absorbance of the solution was measured with UV/Vis spectroscopy (Figure 11).
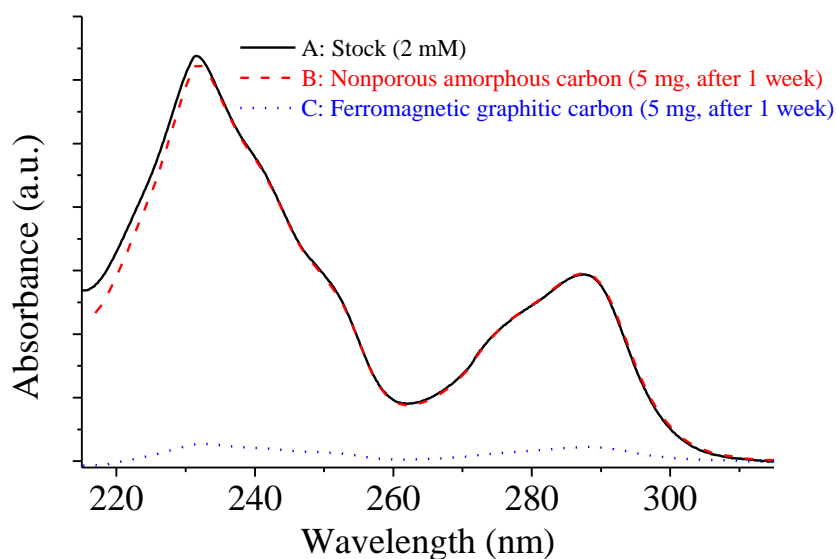
Figure 11 UV/Vis spectrum of a 2 mM aqueous stock solution of compound **1** (A, black), UV\Vis spectrum after 1 week of adsorption with (B, red) nonporous amorphous carbon and (C, blue) ferromagnetic graphitic carbon.

At equilibrium (1 week) an adsorption capacity of 78.13 mg (0.204 mmol) of **1** per g of adsorbent was found. By estimating the surface area of the pyrene scaffold using Chem3D Pro (without the functionality inducing water solubility), the surface coverage could be determined. With a surface area of 0,66 $nm^2 \cdot molecule^{-1}$, the molecules adsorbed amount to approximately 81 m^2, while a surface area of 204 m^2 was available, leading to a surface coverage of approximately 40%, which is in fact a monolayer coverage. The bodies were readily separated from the solution with a conventional neodymium magnet. For comparison an adsorption experiment was executed with 5 mg of carbon bodies obtained from the pyrolysis of MCC in the absence of an iron salt. These bodies virtually showed no adsorption capacity for **1**, which verifies the very low (non-measurable with nitrogen physisorption) surface area found. Both the introduced porosity and the graphitic

content present highly contribute to the adsorption capacity of the ferromagnetic carbon bodies for compound **1**.

Employing smaller (magnetically recoverable) AC bodies will considerably raise the adsorption capacity, particularly for relatively large molecules such as those of natural organic matter (*i.e.* humic acids) with hydrodynamic radii between 2.2 and 6.4 nm [70]. These humic acid molecules are too large to penetrate into the, usual, micropores of the AC, and, consequently, deposit onto the external surface of the AC (shell adsorption mechanism), leading to pore blockage [71]. The use of smaller AC bodies in combination with their ferromagnetic recovery leads thus to a more effective use of the available specific surface area [15] and results in a higher adsorption capacity and rate due to less diffusion limitations with the AC bodies.

4. Conclusions

Catalytic graphitization is used to introduce mesoporosity into amorphous carbon bodies obtained by the pyrolysis of microcrystalline cellulose. Hydrophilic microcrystalline cellulose spheres are easily loaded with various (nitrate, citrate, chloride) iron salts. Pyrolysis leads to the formation of mesoporous ferromagnetic graphitic carbon bodies with attractive properties in view of catalytic and remedial applications. In the course of the pyrolysis the metal salts employed thermally decompose to magnetite (Fe_3O_4), while the cellulose is converted to an amorphous carbonaceous support material. At elevated temperatures, the amorphous carbon is capable to carbothermally reduce the Fe_3O_4 stepwise via wüstite (FeO) to metallic iron nanoparticles. The size and distribution of the iron nanoparticles is affected by the anion of the iron salt. At T > 700 °C the iron nanoparticles recrystallize the amorphous carbon into graphitic carbon nanostructures in which mesoporosity is introduced into the initially non-porous carbon. The extent of

graphitization is influenced by the iron nanoparticle size distribution, which is affected by the anion of the iron salt. For the non-volatile iron salts iron(III) nitrate and ammonium iron(III) citrate nanoparticles are formed. These are active in the catalytic graphitization process leading to mesoporous materials. The increased mesoporosity enhances transport of reactants, products and/or contaminants inside the ferromagnetic graphitic carbon bodies, as shown with the adsorption of an organic pyrene derivative from aqueous solution. The ferromagnetic and remnant free character of the carbon bodies enables magnetic isolation and redispersion which allows for the use of very small carbon bodies in liquid-phase catalysis and remediation further improving transport to the surface and within the mesoporous carbon bodies, while the lubricating properties of the graphitic content provides attrition resistant bodies. In the case of iron(III) chloride large iron particles are obtained due to its volatility. Due to the large size of the iron particles catalytic graphitization is hampered. Therefore no mesopores are being introduced.

Appendix A. Supplementary data

Supplementary data related to this article can be found at http://dx.doi.org/10.1016/j.carbon.xxxx.xx.xxx.

References

[1] Rodríguez-Reinoso, F. The Role of Carbon Materials in Heterogeneous Catalysis. *Carbon* **1998**, *36*, 159-175.

[2] Marsh, H.; Rodríguez-Reinoso, F. Activated Carbon. Elsevier: Amsterdam **2006**.

[3] Bansal, R. C.; Goyal M. Activated Carbon Adsorption. CRC Press: Philadelphia **2005**.

[4] Sing, K. S. W.; Everett, D. H.; Haul, R. A. W.; Moscou, L.; Pierotti, R. A.; Rouquerol. J.; et al. Reporting Physisorption Data for Gas/Solid Systems with Special Reference to the Determination of Surface Area and Porosity. *Pure Appl. Chem.* **1985**, *57*, 603-669.

[5] Rodríguez-Reinoso, F.; Molina-Sabio, M. Activated Carbons from Lignocellulosic Materials by Chemical and/or Physical Activation: An Overview. *Carbon* **1992**, *32*, 1111-1118.

[6] Rodríguez-Reinoso, F.; Molina-Sabio, M.; Gonzalez, M. T. The Use of Steam and CO_2 as Activating Agents in the Preparation of Activated Carbons. *Carbon* **1995**, *33*, 15-23.

[7] Caturla, F.; Molina-Sabio, M.; Rodríguez-Reinoso, F. Preparation of Activated Carbon by Chemical Activation with $ZnCl_2$. *Carbon* **1991**, *29*, 999-1007.

[8] Titirici, M. M.; White, R. J.; Brun, N.; Budarin, V. L.; Su, D. S.; Del Monte, F.; et al. Sustainable Carbon Materials. *Chem. Soc. Rev.* **2015**, *44*, 250-290.

[9] Averill, B. A.; Moulijn, J. A.; Van Santen, R. A.; Van Leeuwen, P. W. N. M. Catalysis: An Integrated Approach. Elsevier: Amsterdam **1999**.

[10] Tseng, R. L.; Tseng, S. K. Pore Structure and Adsorption Performance of the KOH-Activated Carbons Prepared from Corncob. *J. Colloid Interface Sci.* **2005**, *287*, 428-437.

[11] Tsang, S. C.; Caps, V.; Paravskevas, I.; Chadwick, D.; Thompsett, D.; Magnetically Separable, Carbon Supported Nanocatalysts for the Manufacture of Fine Chemicals. *Angew. Chem. Int. Ed.* **2004**, *43*, 5645-5649.

[12] Bandosz, T. J.; Activated Carbon Surfaces in Environmental Remediation. Elsevier: Amsterdam **2006**.

[13] Teunissen, W.; Bol, A. A.; Geus, J. W.; Magnetic Catalyst Bodies. *Catal. Today* **1999**, *48*, 329-336.

[14] Polshettiwar, V.; Luque, R.; Fihri, A.; Zhu, M.; Bouhrara, M.; Basset, J. M. Magnetically Recoverable Nanocatalysts. *Chem. Rev*. **2011**, *111*, 3036-3075.

[15] Ando, N.; Matsui, Y.; Kurotobi, R.; Nakano, Y.; Matsushita, T.; Ohno, K. Comparison of Natural Organic Matter Adsorption Capacities of Super-Powdered Activated Carbon and Powdered Activated Carbon. *Water Res*. **2010**, *44*, 4127-4136

[16] Hoekstra, J.; Versluijs-Helder, M.; Vlietstra, E. J.; Geus, J. W.; Jenneskens, L.W. Carbon-Supported Base Metal Nanoparticles: Cellulose at Work. *ChemSusChem* **2015**, *8*, 985-989.

[17] Hoekstra, J.; Beale, A. M.; Soulimani, F.; Versluijs-Helder, M.; Geus, J. W.; Jenneskens, L. W. Base Metal Catalyzed Graphitization of Cellulose: A Combined Raman Spectroscopy, Temperature Dependent X-ray Diffraction and High-Resolution Transmission Electron Microscopy Study. *J. Phys. Chem. C* **2015**, *119*, 10653-10661.

[18] Huber, D. L. Synthesis, Properties, and Applications of Iron Nanoparticles. *Small* **2005**, *1*, 482-501.

[19] Walker Jr, P.; Rusinko Jr, F.; Austin, L. G. Advances in Catalysis. Academic Press: New York **1959**: Chapter 2:Thermodynamic of Gas-Carbon Reactions, 135-137.

[20] Hunt, J.; Ferrari, A.; Lita, M.; Ashley, B.; Stiegman, A. E. Microwave-Specific Enhancement of the Carbon Dioxide (Boudouard) Reaction. *J. Phys. Chem. C* **2013**, *117*, 26871-26880.

[21] Brunauer, S.; Emmet, H.; Teller, E. Adsorption of Gases in Multimolecular Layers. *J. Am. Chem. Soc. 1938*, **60**, 309-319.

[22] Barrett, E. P.; Joyner, L. G.; Halenda, P. P. The Determination of Pore Volume and Area Distributions in Porous Substances. Computations from Nitrogen Isotherms. *J. Am. Chem. Soc.* **1951**, *73*, 373-380.

[23] Sadezky, A.; Muckenhuber, H.; Grothe, H.; Niessner, R.; Pöschl, U. Raman Microspectroscopy of Soot and Related Carbonaceous Materials: Spectral Analysis and Structural Information. *Carbon* **2005**, *43*, 1731-1742.

[24] Nakashima, N.; Tomonari, Y.; Murakami, H. Water-Soluble Single-Walled Carbon Nanotubes via Noncovalent Sidewall Functionalization with a Pyrene-Carrying Ammonium Ion. *Chem Lett*. **2002**, *31*, 638-639.

[25] Hill, W. D. The Thermal Decomposition of Iron(III) Nitrate Nonahydrate Followed by a Reaction with Hydrogen. *Inorg. Chim. Acta* **1986**, *121*, L33

[26] Wieczorek-Kurow, K.; Kozak, A. The Thermal Decompostion $Fe(NO_3)_3 \cdot 9H_2O$. *J. Therm. Anal. Calorim.* **1999**, *58*, 647-651.

[27] Hussein G. A. M. Physicochemical Investigation of the Decomposition Products of Ammonium Metal Carboxylates: Ammonium Ferric Citrate Hydrate. *Powder Technol.* **1994**, *80*, 265-270.

[28] van den Berg, F. A. Zirconia-Supported Iron-Based Fischer-Tropsch Catalysts, Influence of Pressure and Potassium on Structure and Catalytic Properties. Utrecht University, Utrecht, NL, PhD thesis, **2001**.

[29] Kanungo, S. B.; Mishra, S. K. Thermal Dehydration and Decomposition of $FeCl_3 \cdot xH_2O$ *J. Therm. Anal.* **1996**, *45*, 1487-500.

[30] Lin, X. P.; Jinag, J. Z. Mössbauer Study of Hydrogen Reduction in Fe and FeNi on Silica Supported Catalysts Prepared by Evaporation. *Phys. Status Solidi A.* **1993**, *138*, K35-K39.

[31] Jozwiak, W. K.; Kaczmarek, E.; Maniecki, T.P.; Ignaczak, W.; Maniukiewicz, W. Reduction Behavior of Iron Oxides in Hydrogen and Carbon Monoxide Atmosphere. *Appl. Catal A: Gen.* **2007**, *326*, 17-27.

[32] Zielinski, J.; Zglinicka, L.; Znak, L.; Kaszkur, Z. Reduction of Fe_2O_3 with Hydrogen. *Appl. Catal A: Gen.* **2010**, *381*, 191-196.

[33] Demidov, A.; Markelov, I. Thermodynamics of Formation of Iron Oxides and Their Hydrogen Reduction. *Russ. J. Appl. Chem.* **2010**, *83*, 232-236.

[34] Shen, Y. Carbothermal Synthesis of Metal-Functionalized Nanostructures for Energy and Environmental Applications. *J. Mater. Chem. A.* **2015**, *3*, 13114-131888.

[35] Mamleev. B.; Bourbigot, S.; Yvon, J. Kinetic Analysis of the Thermal Decomposition of Cellulose: the Change of the Rate Limitation. *J. Anal. Appl. Pyr.* **2007**, *80*, 141-150.

[36] Wilson, L. E.; Gregory, N. W. Vapor-Solid Equilibria in the Iron-Chlorine System. *J. Phys. Chem.* **1958**, *62*, 433-437.

[37] Hoekstra, J.; Berben, P. H.; Geus, J. W.; Jenneskens, L. W. A New Procedure to Produce Carbon Supported Metal Catalysts. *Stud. Surf. Sci. Catal.* **2010**, *175*, 93-100.

[38] Tuinstra, F.; Koenig, J. L. Raman Spectrum of Graphite. *J. Chem. Phys.* **1970**, *53*, 1126 - 1130.

[39] Ferrari, A. C.; Robertson, J. Interpretation of Raman Spectra of Disordered and Amorphous Carbon. *J. Phys. Rev. B* **2000**, *61*, 14095-14107.

[40] Gançado, L. G.; Pimenta, M. A.; Neves, B. R.; Dantas, M. S.; Joria, A. Influence of the Atomic Structure on the Raman Spectra of Graphite Edges. *Phys. Rev. Lett.* **2004**, *93*, 247401.

[41] Cuesta, A.; Dhamelincourt, P.; Laureyns, J.; Martínez-Alonso, A.; Tascon, J. M. D. Raman Microprobe Studies on Carbon Materials. *Carbon* **1994**, *32*, 1523-1532.

[42] Jawhari, T.; Roid, A.; Casado, J. Raman Spectroscopic Characterization of Some Commercially Available Carbon Black Materials. *Carbon* **1995**, *33*, 1561-1565.

[43] Dipper, B.; Jander, H.; Heintzenberg, J. NIR FT Raman Spectroscopic Study of Flame Soot. *Phys. Chem. Chem. Phys.* **1999**, *1*, 4707-4712.

[44] Lespade, P.; Marchand, A.; Couzi, M.; Cruege, F. Characterisation de Materiaux Carbones Par Microspectrometrie Raman. *Carbon* **1984**, *22*, 375-385.

[45] Escribano, R.; Sloan, J. J.; Siddique, N.; Sze, N.; Dudev, T. Raman Spectroscopy of Carbon-Containing Particles. *Vib. Spectrosc.* **2001**, *26*, 179-186.

[46] Sze, S. K.; Siddique, N.; Sloan, J. J.; Escribano, R. Raman Spectroscopic Characterization of Carbonaceous Aerosols. *Atmos. Environ.* **2001**, *35*, 561-568.

[47] Malard, L. M.; Pimenta, M. A.; Dresselhaus, G.; Dresselhaus, M. S. Raman Spectroscopy in Graphene. *Phys. Rep.* **2009**, *473*, 51-87.

[48] Ferrari, A. C. Raman Spectroscopy of Graphene and Graphite: Disorder, Electron-Phonon Coupling, Doping and Nonadiabatic Effects. *Solid State Commun.* **2007**, *143*, 47-57.

[49] Bleyl, S.; Kopinke, F. D.; Mackenzie, K. Carbo-Iron® - Synthesis and Stabilization of $Fe^{(0)}$-Doped Colloidal Activated Carbon for In Situ Groundwater Treatment. *Chem. Eng. J.* **2012**, *191*, 588-595.

[50] Huidobro, A.; Pastor, A.C.; Rodríguez-Reinoso, F. Preparation of Activated Carbon Cloth from Viscous Rayon: Part IV. Chemical Activation. *Carbon* **2001**, *39*, 389-398.

[51] Kyotani, T. Control of Pore Structure in Carbon. *Carbon* **2000**, *38*, 269-286.

[52] Lee, J.; Kim, J.; Hyeon, T. Recent Progress in the Synthesis of Porous Carbon Materials. *Adv. Mater.* **2006**, *18*, 2073-2094.

[53] Oya, A.; Yoshida, S.; Alcaniz-Monge, J.; Linares-Solano, A. Formation of Mesopores in Phenolic Resin-Derived Carbon Fiber by Catalytic Activation Using Cobalt. *Carbon* **1995**, *33*, 1085-1090.

[54] Iwazaki, T.; Semba, T.; Konishi, S.; Sezai, T.; Murakami, Y.; Sugimoto, W.; et al. Catalytic Excavation and Graphitization of Activated Carbon by Cobalt Nanoparticles. *Chem. Lett.* **2008**, *37*, 1194-1195.

[55] Zhai, D.; Du, H.; Li, B.; Shu, Y.; Kang, F. Porous Graphitic Carbons Prepared by Combining Chemical Activation with Catalytic Graphitization. *Carbon* **2011**, *49*, 725-729.

[56] Thompson, E.; Danks, A.E.; Bourgeois, L.; Schnepp, Z. Iron Catalyzed Graphitization of Biomass, *Green Chem.* **2015**, *17*, 551-556.

[57] Baldovino-Medrano, Le M. T.; Van Driessche, I.; Bruneel, E.; Gaigneaux, E. M. Influence of Graphite as a Shaping Agent of Bi Molybdate Powders on Their Mechanical, Physicochemical, and Catalytic Properties. *Ind. Eng. Chem. Res.* **2011**, *50*, 5467-5477.

[58] Shylesh, S.; Schunemann, V.; Tiel, W. R. Magnetically Separable Nanocatalysts: Bridges Between Homogeneous and Heterogeneous Catalysis. *Angew. Chem. Int. Ed.* **2010**, *49*, 3428-3459.

[59] Gustavson, P.; A Thermodynamic Evaluation of the Fe-C System. *Scand. J. Metall.* **1985**, *14*, 259-267.

[60] Sohn, K.; Kang, S. W.; Ahn, S.; Woo, M.; Yang, S. K. Fe[(0)] Nanoparticles for Nitrate Reduction: Stability, Reactivity and Transformation. *Environ. Sci. Technol.* **2006**, *40*, 5514-5519.

[61] Tsuzuki, A.; Sago, S.; Hirano, S. I.; Naka, S. High Temperature and Pressure Preparation and Properties of Iron Carbides Fe_7C_3 and Fe_3C. *J. Mater. Sci.* **1984**, *19*, 2513-2518.

[62] Meffre, A.; Mehdaoui, B.; Kelsen, V.; Fazzini, P. F.; Carrey, J.; Lachaize, S.; et al. Simple Chemical Route Toward Monodisperse Iron Carbide Nanoparticles Displaying Tunable Magnetic and Unprecedented Hyperthermia Properties. *Nano Lett.* **2012**, *12*, 4722-2478.

[63] Frey, N.A.; Peng, S.; Cheng, K.; Sun, S. Magnetic Nanoparticles: Synthesis, Functionalization, and Applications in Bioimaging and Magnetic Energy Storage. *Chem. Soc. Rev.* **2009**, *38*, 2532-2542.

[64] Schlögl, R. Catalytic Synthesis of Ammonia - a "Never-Ending Story"? *Angew. Chem. Int. Ed.* **2003**, *42*, 2004-2008.

[65] De Smit, E.; Weckhuysen, B. M. The Renaissance of Iron-Based Fischer–Tropsch Synthesis: on the Multifaceted Catalyst Deactivation Behaviour. *Chem. Soc. Rev.* **2008**, *37*, 2758-2581.

[66] De Jong, K. P.; Geus, J. W. Carbon Nanofibers: Catalytic Synthesis and Applications. *Catal. Rev. Sci. Eng.* **2000**, *42*, 481-510.

[67] Wittmann, S.; Schätz, A.; Grass, R. N.; Stark, W. J.; Reiser, O. A Recyclable Nanoparticle-Supported Palladium Catalyst for the Hydrocarbonylation of Aryl Halides in Water. *Angew. Chem. Int. Ed.* **2010**, *49*, 1867-1870.

[68] Schätz, A.; Grass, R. N.; Stark, W. J.; Reiser, O. TEMPO Supported in Magnetic C/Co-Nanoparticles: A Highly Active and Recyclable Organocatalyst. *Chem. Eur. J.* **2008**, *14*, 8262-8266.

[69] Yang, K.; Zhu, L.; Xing, B. Adsorption of Polycyclic Aromatic Hydrocarbons by Carbon Nanomaterials. *Environ. Sci. Technol.* **2006**, *40*, 1855–1861.

[70] Kawahigashi, M.; Sumida, H.; Yamamoto, K. Size and Shape of Soil Humic Acids Estimated by Viscosity and Molecular Weight. *J. Colloid Interface Sci.* **2005**, *284*, 463-469.

[71] Li, Q.; Snoeyink, V. L.; Marinas, B. J.; Campos, C. Pore Blockage Effect of NOM on Atrazine Adsorption Kinetics of PAC: the Roles of PAC Pore Size Distribution and NOM Molecular Weight. *Water Res.* **2003**, *37*, 4863-4672.